



## OPEN ACCESS

## EDITED BY

Liangliang Lu,  
Nanjing Normal University, China

## REVIEWED BY

Xinzhong Li,  
Henan University of Science and  
Technology, China  
Xinxing Zhou,  
Hunan Normal University, China  
Guanghai Liu,  
Guangdong Polytechnic Normal  
University, China

## \*CORRESPONDENCE

L. M. Pérez,  
lperez@academicos.uta.cl

## SPECIALTY SECTION

This article was submitted to Optics  
and Photonics,  
a section of the journal  
Frontiers in Physics

RECEIVED 12 May 2022

ACCEPTED 27 June 2022

PUBLISHED 26 August 2022

## CITATION

Kria M, Nautiyal VV, Lakaal K,  
El Hamdaoui J, Pérez LM, Varsha,  
Laroze D, Prasad V, Long G and Feddi E  
(2022), Rashba effect on linear and  
nonlinear optical properties of a  
cylindrical core/shell heterojunction  
quantum dot.  
*Front. Phys.* 10:942758.  
doi: 10.3389/fphy.2022.942758

## COPYRIGHT

© 2022 Kria, Nautiyal, Lakaal, El  
Hamdaoui, Pérez, Varsha, Laroze,  
Prasad, Long and Feddi. This is an open-  
access article distributed under the  
terms of the [Creative Commons  
Attribution License \(CC BY\)](https://creativecommons.org/licenses/by/4.0/). The use,  
distribution or reproduction in other  
forums is permitted, provided the  
original author(s) and the copyright  
owner(s) are credited and that the  
original publication in this journal is  
cited, in accordance with accepted  
academic practice. No use, distribution  
or reproduction is permitted which does  
not comply with these terms.

# Rashba effect on linear and nonlinear optical properties of a cylindrical core/shell heterojunction quantum dot

M. Kria<sup>1,2</sup>, Vijit V. Nautiyal<sup>3</sup>, K. Lakaal<sup>1,2</sup>, J. El Hamdaoui<sup>1,2</sup>,  
L. M. Pérez<sup>4\*</sup>, Varsha<sup>3,5</sup>, D. Laroze<sup>6</sup>, V. Prasad<sup>7</sup>, G. Long<sup>8</sup> and  
E. Feddi<sup>1,9</sup>

<sup>1</sup>Group of Optoelectronic of Semiconductors and Nanomaterials, ENSAM, Mohammed V University in Rabat, Rabat, Morocco, <sup>2</sup>Laboratory of Condensed Matter and Interdisciplinary Sciences (LaMCScl), Faculty of Sciences Rabat, Mohammed V University in Rabat, Morocco V University in Rabat, Rabat, Morocco, <sup>3</sup>Department of Physics and Astrophysics, University of Delhi, Delhi, India, <sup>4</sup>Departamento de Física, FACL, Universidad de Tarapacá, Arica, Chile, <sup>5</sup>Department of Physics, Kalindi College, University of Delhi, Delhi, India, <sup>6</sup>Instituto de Alta Investigación, CEDENNA, Universidad de Tarapacá, Arica, Chile, <sup>7</sup>Department of Physics, Swami Shradhanand College, University of Delhi, Delhi, India, <sup>8</sup>Department of Physics, St. John's University, Jamaica, NY, United States, <sup>9</sup>Institute of Applied Physics, Mohammed VI Polytechnic University, Ben Guerir, Morocco

Rashba effect may play an important role in the nonlinear optical properties of heterojunction quantum dots. In this work, we have theoretically examined the effects of Rashba spin-orbit interaction on an electron in a cylindrical core/shell quantum dot (CCSQD). The modifications of various properties of cylindrical core/shell quantum dot such as transition energies, dipole transition matrix elements and linear and nonlinear optical properties due to change in Rashba coupling parameter, magnetic field and effective Rydberg energy were studied. We solved the Schrödinger equation using numerical methods and obtained energy eigenvalues as functions of the aforementioned parameters. It was observed that, the magnetic field has a considerable effect on absorption coefficients and refractive index. It was also observed that increasing the magnetic field shifts the resonances towards higher energies. Additionally, increasing in the Rashba coupling coefficient ( $\alpha_R$ ) was found out to result an increase in absorption coefficients and refractive index. Our results demonstrated that, we can manipulate optical properties of cylindrical core/shell quantum dot using an external magnetic field.

## KEYWORDS

core/shell, quantum dots, Rashba effect, external magnetic field, nonlinear optical properties

## 1 Introduction

In the last decade, heterojunctions formed by heterogeneous semiconductors with different bandgaps have been the focus of attention of researchers in the field of optoelectronics and solid-state devices. Low dimension systems of heterojunction semiconductors provide an extra degree of freedom which opens the door to novel phenomena that are not possible with homogeneous structures [1]. Nanoscale heterostructure-based optoelectronic devices enable precise control over the fundamental properties such as the width of the bandgap, refractive index, effective mass and mobility of charge carriers, and the energy spectrum of electrons. These nanostructures have a diverse range of applications. GaMnAs-based ferromagnetic semiconductors are the most popular systems for investigating spin-dependent transport phenomenon [2]. Double heterostructure (DH) based lasers were developed because, unlike homojunction lasers, they could provide uninterrupted lasing action at high temperatures due to the fact that DH structures have the capacity to attain a high density of carrier injection and population inversion by “double injection” [3]. Semi-insulating heterogeneous semiconductor nanostructures are used for insulated device isolation in integrated circuits and as the current impeding layer in heterostructure lasers due to their high resistivity, short carrier lifetime, and enhanced defect densities [4]. Heterojunction based semiconductor nanostructures are commonly used in various devices such as solar cells [5], gas sensors [6], bipolar transistors [7], wide-dynamic-range image sensors [8] and photocatalysts [9].

Low dimensional (LD) systems of heterojunction structures made with semiconductors are often utilized to confine the motion of charge carriers in one dimension (1D), two dimensions (2D), or in all three dimensions (3D), according to the dimensions of low dimensional systems. Depending on the dimensions of quantum confinement of charge carriers, we can create quantum wells (1D confinement), quantum wires (2D confinement), or quantum dots (3D confinement) [10]. LD systems grant a wide range of functionality to nanoelectronic devices. For instance, recently, researchers working in the field of artificial intelligence have utilized structural, compositional, and chemical tunability of such systems to create advanced neuromorphic devices [11]. These exceptional properties of LD systems help in the fabrication of nanostructures with precisely designed density-of-states which results in increased optical efficiency [12]. One such heterojunction LD system that has played a crucial role in the advancement of semiconductor-based devices is a quantum dot (QD). Quantum dots are quasi-zero dimensional (0D) structures that have discreet atom-like energy levels. The atom-like energy structure of QDs produces a vivid optical spectrum [13] and a few carrier arrangements help us to obtain ultimate control over carrier densities [14]. There have been recent studies that have reported manipulation of spin

states [15] and optical properties [16] of quantum dots by using different parameters such as laser field and wetting layer elements, respectively. Spin states of coupled single-electron quantum dots have been proposed to implement one, and two quantum-bit gates for quantum computing [17]. Gao et al. proposed a groundbreaking study where they describe the development of nanoparticle probes based on semiconductor QD for cancer targeting and imaging [18]. Y.Z. Hu et al. used theoretical and experimental results to provide the first indication of the existence of biexciton states in QDs [19]. Nonlinear optical properties enable us to utilize quantum heterostructures in a wide range of applications incorporating high-order harmonic generation, multi-photon imaging, and optical parametric oscillations [20]. Due to the carrier confinement in low dimension systems, the nonlinear optical response of quantum dots presents an exciting field of study with promising applications. Miller and Chemla considered phonon broadening in QDs and proved that strong local field effects could provide optical bistability without any extrinsic feedback [21]. In colloidal quantum dots, nonlinear optical properties have also been found to strongly influence spectral luminescence [22]. Second-harmonic generation (SHG) has also been observed when placing an impurity on the repulsive part of the confining potential in 2-D quantum rings [23].

Core-shell quantum dots (CSQDs) have been researched extensively due to the fact that their linear and nonlinear properties can be manipulated by controlling the thickness, impurity, and dielectric environment of the shell. For instance, in ZnO/ZnS CSQD, increasing the shell width results in a redshift of threshold energy and a significant rise in nonlinear absorption coefficients as well [24]. Shell thickness can also be used to optimize charge separation yield, lifetime, and recombination rates in CSQDs [25]. CSQD can also be used to create unique quantum structures. For example, by introducing an inorganic semiconducting layer over the CSQD having a bandgap higher than that of the shell, a novel quantum structure called quantum dot quantum well (QDQW) can be fabricated [26]. In GaN/AlN CSQD, it has been observed that in addition to shell thickness, hydrostatic pressure can also be used to modify the nonlinear optical properties [27].

In recent years the studies that involve manipulation of spin in QDs are being focused with plenty of attention due to possible applications of spintronics in futuristic devices [28–30]. The peculiar features of spin-based devices, such as low power consumption, high degree of functionality, etc., provide superiority over the properties based on the electronic charge devices. In spintronic devices, the Spin-Orbit Interactions (SOIs) play an essential role in designing the devices. The two distinct SOIs, namely Rashba and the Dresselhaus effects, are either present in the crystals or are induced by external fields. Depending on the asymmetries involved, either or both play a dominant role in the spin manipulation [31]. Indeed, the Rashba term is considered as the momentum-depend splitting of the spin

band in both systems: bulk and low dimensional systems (heterostructures, surface states, and QD). This spin-orbit coupling is independent of structures of the shape or geometry. For more details, we refer the readers to Refs. [32–36].

Let us comment that Pan Sun et al. [37] have reported optical and magnetic properties of doped wide-band-gap GaN. They have shown that the photoluminescence (PL) intensity increased under an external magnetic field. This issue may open up a suite of potential applications in producing magneto-optical devices. More recently, Mkrtchyan et al. [38] have studied the interband and intraband optical transitions in an asymmetric bi convex lens-shaped QD made in InAs in the presence of an external magnetic field. The authors have demonstrated a broadening of the absorption peaks with increasing temperature and a decrease in the peaks amplitudes with magnetic field strength increases. They have shown that the SHG and THG nonlinear parameters of the system decreased with an increase in the magnetic field.

A significant study concerning the magneto-refractive effects of PbS quantum dots (QDs) core fiber with different particle sizes was investigated using the DFT method [39]. The defect structures of PbS nanoclusters were constructed, and the spin magnetic moments of sulfur (S) and plumbum (Pb) were analyzed. In this study, the authors show that the magnetic moments are mainly induced by the spin interaction between Pb 6s, 6p, and S 3p states. In addition, they have demonstrated that spin magnetism shows a weakening trend as the particle size increases. Their experimental investigations show that the magneto-refractive effect is strong as the size of PbS QDs decreases which indicates that this material can be used for magnetic field sensing applications.

On the other hand, we understand that advances in fabrication of nanoscale structures such as molecular beam epitaxy and metal oxide chemical vapor deposition has made it possible to design the quantum heterostructures of required shapes and sizes. So fabrication of cylindrical core/shell Quantum dot experimentally a possibility [40–42]. Recently Iorio et al [43] reported experimental results on suspended Quantum wire in external magnetic field where they have manipulated the orientation of Spin-Orbit interactions in external magnetic field. Of course the magnetic field strength in their case is quite small. Also there are experimental realisations where spin-orbit couplings are studied experimentally on nanowires [44, 45]. In view of the above, we can conclude that the study undertaken here can be studied experimentally.

In the present work, we study a GaN/AlN cylindrical core-shell quantum dot (CCSQD) while including the effects of Rashba SOI and using the finite element method to obtain the eigenvalues of the electron in the CCSQD. After finding the energy eigenvalues, we calculated the changes in absorption coefficients (AC) and the refractive index (RI). We used the compact density matrix and perturbation theory approach for this. Finally, we find second harmonic generation (SHG) and third harmonic generation (THG) susceptibilities, respectively.

Our motivation was to study the variations in the aforementioned physical properties with changes in the Rashba parameter, Rydberg free energy, and the magnetic field.

## 2 Theory

### 2.1 Electronic properties

We will consider an electron confined in a single GaN/AlN CCSQD, which is structured such that a large band offset exists between core and shell materials, as in GaN/AlN ( $E_g^{GaN} = 3.4 \text{ eV}$ ) [46]. The single QDs are surrounded by the dielectric material shell with large band gap. Therefore, infinite confining potentials can be considered as a good approximation for our model. The structure is submitted to a uniform magnetic field directed along to the z-axis.

In the frame work of Effective Masse Approximation (EMA), the Hamiltonian of the system, which considers the effects of the Zeeman and Rashba effects can be written as:

$$\mathcal{H} = \mathcal{H}_0 + \frac{1}{2}g^*\mu_B B\sigma_z + \mathcal{H}_R \quad (1)$$

where  $\mathcal{H}_0$  is the unperturbed Hamiltonian of a single-particle electron in a CCSQD:

$$\mathcal{H}_0 = \frac{1}{2m_e^*} \left( \vec{p} - \frac{e}{c} \vec{A} \right)^2 + V_w(r_e) \quad (2)$$

with  $\vec{A} = B/2(-y, x, 0)$  the vector potential corresponding to the applied magnetic field expressed in the Coulomb gauge,  $m_e^*$  is the effective mass of the electron,  $e$  is the absolute value of the electron charge. In the structures where the band offsets between the core and shell materials is very important, the electron confining potentials in the xy-plane  $V(\rho_e)$  and in the z-direction  $V(z_e)$  were assumed the following forms [48]:

$$V_w(\rho_e) = \begin{cases} 0 & \text{for } R_c \leq \rho_e \leq R_s \\ \infty & ; \text{ otherwise} \end{cases} \text{ and} \quad (3)$$

$$V_w(z_e) = \begin{cases} 0 & \text{for } |z| \leq \frac{H}{2} \\ \infty & ; \text{ otherwise} \end{cases}$$

The second term in the Hamiltonian [1] describes the Zeeman contribution where  $g^*$  is the Landé g factor for the bound electron,  $\mu_B$  is the Bohr magneton,  $\sigma_z$  is the z component of the Pauli matrices vector  $\sigma$ .  $\mathcal{H}_R$  is the 2D Rashba spin-orbit interaction Hamiltonian.

$$\mathcal{H}_R = \frac{\alpha_R}{\hbar} \left[ \hat{\sigma} \times \left( \hat{p} - \frac{e}{c} \hat{A} \right) \right] \quad (4)$$

Where  $\alpha_R$  is Rashba SOI parameter.

With the introduction of the RSOI, the Hamiltonian of the system is expressed as a  $2 \times 2$  matrix as follows:

$$\begin{pmatrix} \mathcal{H}_{11} & \mathcal{H}_{12} \\ \mathcal{H}_{21} & \mathcal{H}_{22} \end{pmatrix} \Psi_e = E_{\pm} \Psi_e \quad (5)$$

Where  $\Psi_e = \Psi_{\uparrow} \begin{pmatrix} 1 \\ 0 \end{pmatrix} + \Psi_{\downarrow} \begin{pmatrix} 0 \\ 1 \end{pmatrix}$  are the eigenstates of the system.  $\begin{pmatrix} 1 \\ 0 \end{pmatrix}$  and  $\begin{pmatrix} 0 \\ 1 \end{pmatrix}$  are the eigenfunctions of  $\sigma_z$ .  $\Psi_{\uparrow}$  and  $\Psi_{\downarrow}$  are the wave functions with spin-up and spin-down, respectively. The matrix elements of the equation [5] are:

$$\begin{aligned} \mathcal{H}_{11} = & \frac{-\hbar^2}{2m_e^*} \left( \frac{\partial^2}{\partial x^2} + \frac{\partial^2}{\partial y^2} + \frac{\partial^2}{\partial z^2} \right) + \frac{e^2 B^2}{8m_e^* c^2} (x^2 + y^2) \\ & + \frac{ieB\hbar}{2m_e^* c} \left( x \frac{\partial}{\partial y} - y \frac{\partial}{\partial x} \right) + \frac{1}{2} g^* \mu_B B + V_w^e(x, y) \end{aligned} \quad (6)$$

$$\begin{aligned} \mathcal{H}_{22} = & \frac{-\hbar^2}{2m_e^*} \left( \frac{\partial^2}{\partial x^2} + \frac{\partial^2}{\partial y^2} + \frac{\partial^2}{\partial z^2} \right) + \frac{e^2 B^2}{8m_e^* c^2} (x^2 + y^2) \\ & + \frac{ieB\hbar}{2m_e^* c} \left( x \frac{\partial}{\partial y} - y \frac{\partial}{\partial x} \right) - \frac{1}{2} g^* \mu_B B + V_w^e(x, y) \end{aligned} \quad (7)$$

$$\mathcal{H}_{12} = \alpha_R \left( \frac{\partial}{\partial x} - i \frac{\partial}{\partial y} - \frac{eB}{2\hbar c} (x + iy) \right) \quad (8)$$

$$\mathcal{H}_{21} = -\alpha_R \left( \frac{\partial}{\partial x} + i \frac{\partial}{\partial y} + \frac{eB}{2\hbar c} (-x + iy) \right) \quad (9)$$

In cylindrical coordinate system, the energy and the wave function are given by the solutions of Schrödinger equation  $\mathcal{H}\Psi_e(\rho, \varphi, z) = E\Psi_e(\rho, \varphi, z)$ , we remark that the Hamiltonian of the system can be written as a sum of the two independent parts:

$$[\mathcal{H}(\rho, \varphi) + \mathcal{H}(z)]\Psi_e(\rho, \varphi, z) = E\Psi_e(\rho, \varphi, z) \quad (10)$$

It is worth mentioning that, the application of the EMA constitute an important debate in strong confinement characterized by the sizes less than  $a^*$ . This approximation is only questionable when it is coupled with the variational method. In our case, even if we use the EMA, the resolution of the Schrödinger equation is done by using the finite element method which gives a very close results to other method as tight binding or kp theory mainly when we use an Extra-fine meshing. As a result, the wave function can be expressed as a product of the two independent parts:

$$\Psi_e(\rho, \varphi, z) = F(\rho, \varphi)g(z) \quad (11)$$

Substituting the wave function (Eq. 11) in Eq. 10, we obtained the following equations

$$\begin{aligned} & \left[ \frac{-\hbar^2}{2m_e^*} \left( \frac{\partial^2}{\partial \rho^2} + \frac{1}{\rho} \frac{\partial}{\partial \rho} + \frac{1}{\rho^2} \frac{\partial^2}{\partial \varphi^2} \right) - \frac{eB\hbar}{2m_e^* c^2} L_z + \frac{e^2 B^2}{8m_e^* c^2} \rho^2 \right] F(\rho, \varphi) \\ & = E_{\rho} F(\rho, \varphi) \end{aligned} \quad (12)$$

Using variable separation, we obtained:

$$\left[ \frac{-\hbar^2}{2m_e^*} \left( \frac{\partial^2}{\partial \rho^2} + \frac{1}{\rho} \frac{\partial}{\partial \rho} - \frac{m^2}{\rho^2} \right) - \frac{eB\hbar}{2m_e^* c^2} m + \frac{e^2 B^2}{8m_e^* c^2} \rho^2 \right] R(\rho) = E_{\rho} R(\rho) \quad (13)$$

Using the effective atomic unit, we can rewrite the Bohr radius as  $a^* = \hbar^2 \epsilon / m_e^* e^2$  and effective Rydberg energy as  $R^* = \hbar^2 / 2m_e^* (a^*)^2$ . In these units, the Hamiltonian of our system can be written as:

$$-\left( \frac{\partial^2}{\partial \rho^2} + \frac{1}{\rho} \frac{\partial}{\partial \rho} \right) F(\rho) + \left( \frac{m^2}{\rho^2} + \frac{\gamma^2 \rho^2}{4} \right) F(\rho) - (E_{\rho} + m\gamma) F(\rho) = 0 \quad (14)$$

and

$$-\frac{\partial^2}{\partial z^2} g(z) = E_z g(z) \quad (15)$$

Where  $\gamma = \frac{\hbar \omega_c}{2R^*}$  and  $\omega_c = \frac{eB}{m_e^* c}$  is the effective cyclotron frequency. The solutions of Eqs 14, 15 are as follows:

$$F(\rho) = \frac{1}{\rho} \left[ A W_{t,m/2} \left( \frac{\gamma \rho^2}{2} \right) + B M_{t,m/2} \left( \frac{\gamma \rho^2}{2} \right) \right] \quad (16)$$

Where  $t = m + \frac{E_{mm}}{2\gamma}$  and

$$g(z) = \sin \left( \frac{l\pi z}{H} + \frac{l\pi}{2} \right) \quad (17)$$

Here, A and B are constants that can be obtained by boundary conditions and through normalization of the wave functions. Also,  $W_{t,m/2} \left( \frac{\gamma \rho^2}{2} \right)$  and  $M_{t,m/2} \left( \frac{\gamma \rho^2}{2} \right)$  are the Whittaker function of first and second class, whereas,  $W_{m/2}$  and  $M_{m/2}$  are the mth-order Whittaker function. We recall that the radial wave function must vanish at the inner ( $\rho = a$ ) and outer ( $\rho = b$ ) radial boundary. These conditions are introduced by the following transcendental equation

$$\left[ W_{t,m/2} \left( \frac{\gamma a^2}{2} \right) M_{t,m/2} \left( \frac{\gamma b^2}{2} \right) - M_{t,m/2} \left( \frac{\gamma a^2}{2} \right) W_{t,m/2} \left( \frac{\gamma b^2}{2} \right) \right] = 0 \quad (18)$$

The electron eigenenergies are related to the parameters  $E_{mn}$  by the following relation:

$$E_{lmm} = \left[ E_{mn}^2 + \left( \frac{l\pi}{H} \right)^2 \right]; \quad l = 1, 2, \dots, \quad m = 0, \pm 1, \pm 2, \dots \quad (19)$$

Now, we consider the Rashba Hamiltonian and write the Schrodinger equation of the system as

$$\begin{pmatrix} H_0 + \frac{1}{2} g^* \mu_B B & H_{12}^R \\ H_{21}^R & H_0 - \frac{1}{2} g^* \mu_B B \end{pmatrix} \begin{pmatrix} C_+ \Psi_+ \\ C_- \Psi_- \end{pmatrix} = E_{\pm} \begin{pmatrix} C_+ \Psi_+ \\ C_- \Psi_- \end{pmatrix} \quad (20)$$

where

$$\begin{aligned} H_{21}^R &= \alpha_R e^{-i\varphi} \left[ \frac{\partial}{\partial \rho} - \frac{i}{\rho} \frac{\partial}{\partial \varphi} + \frac{eB}{2\hbar} \rho \right] \\ H_{12}^R &= \alpha_R e^{i\varphi} \left[ -\frac{\partial}{\partial \rho} - \frac{i}{\rho} \frac{\partial}{\partial \varphi} + \frac{eB}{2\hbar} \rho \right] \end{aligned} \quad (21)$$

and  $C_+$ ,  $C_-$  are the expansion coefficients.

One can obtain the following system of algebraic equations if we let  $\Phi(\rho, z) = F(\rho)g(z)$

$$\begin{aligned} \left[ E_{imm} - E_{\pm} + \frac{1}{2}g^* \mu_B B \right] C_{\pm} \Phi(\rho, z) + \alpha_R \left[ \frac{\partial}{\partial \rho} + \frac{m+1}{\rho} + \frac{eB}{2\hbar\rho} \right] C_{\pm} \Phi(\rho, z) &= 0 \\ \left[ E_{imm} - E_{\pm} - \frac{1}{2}g^* \mu_B B \right] C_{\pm} \Phi(\rho, z) + \alpha_R \left[ -\frac{\partial}{\partial \rho} + \frac{m}{\rho} + \frac{eB}{2\hbar\rho} \right] C_{\pm} \Phi(\rho, z) &= 0 \end{aligned} \tag{22}$$

We have multiplied the system equations by  $\Phi^*(\rho, z)$  integrating over the whole space and used the above relations to obtain the energy eigenvalues  $E_{\pm}$ .

## 2.2 Nonlinear optical properties

In this section, we recall the main results of the electric-dipole approximation that describes a transition from the ground state to the first excited state. Since this theory is a natural extension of a well-known theory of the optical absorption [49, 50], we will only present its main results. By neglecting the influence of the temperature and restricting the calculation only to one-photon transitions at 0K, we determined the optical absorption coefficients (ACs) and the refractive index changes (RICs). Generally speaking, this designation one photon transition at 0 K is usually used when the phonons effect is neglected. In a monochromatic electromagnetic field with frequency  $\omega$ , the transition probability between two states  $i$  and  $f$  is generally known as the oscillator strength and can be given by the Fermi golden rule. The mathematical formulations for linear photoabsorption coefficient ( $\alpha^{(1)}$ ) and the third-order nonlinear photoabsorption coefficient ( $\alpha^{(3)}$ ) have been derived from the density matrix approach and the perturbation theory. Thus, the expression for  $\alpha$ , the total absorption coefficient (AC) is as follows [48, 51, 52]:

$$\alpha(\omega, I) = \alpha^{(1)}(\omega) + \alpha^{(3)}(\omega, I), \tag{23}$$

Where,

$$\alpha^{(1)}(\omega) = \omega \sqrt{\frac{\mu}{\epsilon}} \frac{\hbar \Gamma_{fi} |M_{fi}|^2 \sigma}{(E_{fi} - \hbar\omega)^2 + (\hbar\Gamma_{fi})^2} \tag{24}$$

and

$$\begin{aligned} \alpha^{(3)}(\omega, I) = -\omega \sqrt{\frac{\mu}{\epsilon}} \left( \frac{I}{2\epsilon_0 n_r c} \right) \frac{4\sigma \hbar \Gamma_{fi} |M_{fi}|^4}{[(E_{fi} - \hbar\omega)^2 + (\hbar\Gamma_{fi})^2]^2} \\ \left[ 1 - \frac{(M_{ff} - M_{ii})^2}{4|M_{fi}|^2} \left\{ \frac{3E_{fi}^2 - 4\hbar\omega E_{fi} + \hbar^2(\omega^2 - \Gamma_{fi}^2)}{E_{fi}^2 + (\hbar\Gamma_{fi})^2} \right\} \right] \end{aligned} \tag{25}$$

where  $E_{fi} = E_f - E_i$  denotes the energy transition between an initial state ( $i$ ) and a final state ( $f$ ).  $M_{fi} = e \langle \Psi_f | \rho | \Psi_i \rangle$  is the transition matrix element between the state  $i$  and state  $f$ . Note that the parameters used above are:  $c$  is the speed of light in a vacuum,  $\sigma_s$  is the electron density related to the occupied volume by the relation,  $I$  is the intensity of the incident electromagnetic

radiation,  $\omega$  is the angular frequency of the laser radiation,  $\mu$  is the permeability of the system,  $n_r$  is the relative refractive index of semiconductor and  $\epsilon_0$  is the permittivity of the free space  $\Gamma_{fi}$  is the line width which is also defined as the inverse of the relaxation time  $\tau_{fi}$  and known as the relaxation rate of initial and final states. It was found that the propagation of electromagnetic radiation through a material also produces changes in the refractive index of the material. The sum of linear and nonlinear third-order refractive index change is denoted as the total refractive index change (RIC).

$$\frac{\Delta n(\omega)}{n_r} = \frac{\Delta n^{(1)}(\omega)}{n_r} + \frac{\Delta n^{(3)}(\omega)}{n_r} \tag{26}$$

Where,

$$\frac{\Delta n^{(1)}(\omega)}{n_r} = \frac{1}{2\epsilon_0 n_r^2} \frac{\sigma |M_{fi}|^2 (E_{fi} - \hbar\omega)}{(E_{fi} - \hbar\omega)^2 + (\hbar\Gamma_{fi})^2} \tag{27}$$

and

$$\begin{aligned} \frac{\Delta n^{(3)}(\omega, I)}{n_r} = -\frac{\mu c I \sigma |M_{fi}|^4}{\epsilon_0 n_r^3} \frac{(E_{fi} - \hbar\omega)}{[(E_{fi} - \hbar\omega)^2 + (\hbar\Gamma_{fi})^2]^2} \\ \times \left[ 1 - \frac{(M_{ff} - M_{ii})^2}{4|M_{fi}|^2 (E_{fi}^2 + (\hbar\Gamma_{fi})^2)} \times \{E_{fi}(E_{fi} - \hbar\omega) - (\hbar\Gamma_{fi})^2 \right. \\ \left. - (\hbar\Gamma_{fi})^2 \times \frac{(2E_{fi} - \hbar\omega)}{(E_{fi} - \hbar\omega)} \right] \end{aligned} \tag{28}$$

To have a complete description of the nonlinear optical responses of a system excited by an electromagnetic radiation  $E(t) = E_0 e^{j(\omega t)} + E_0 e^{-j(\omega t)}$  polarized along the z-axis, we used the development of the polarization as power series of the field strength.

$$P(t) \equiv \epsilon_0 [\chi_{\omega}^{(1)} E(t) + \chi_{\omega}^{(2)} E^2(t) + \chi_{\omega}^{(3)} E^3(t) + \dots] \tag{29}$$

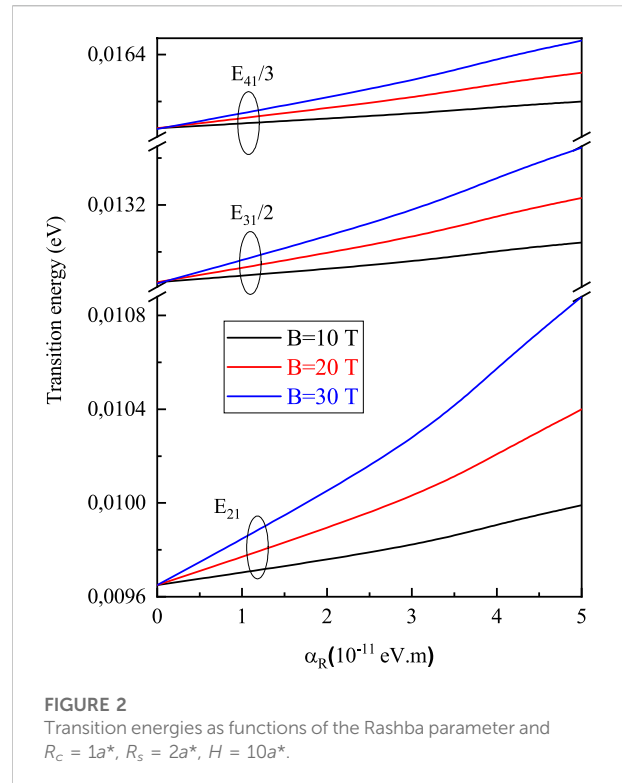
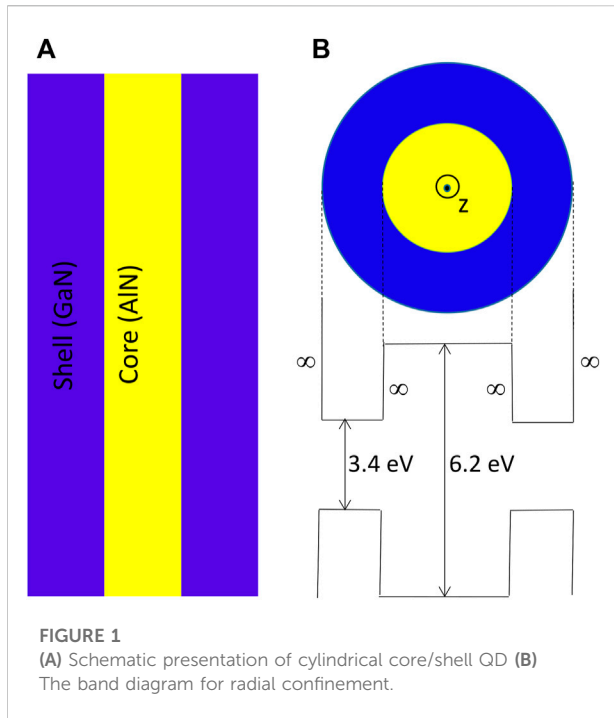
where  $\chi_{\omega}^{(1)}$  is the linear susceptibility while  $\chi_{\omega}^{(2)}$  and  $\chi_{\omega}^{(3)}$  are defined as the second and third order nonlinear optical susceptibilities.

The partial development of Eq. 29 leads to the usual expansion:

$$\begin{aligned} P(t) = \epsilon_0 \chi_{\omega}^{(1)} E_0 e^{i\omega t} + \epsilon_0 \chi_0^{(2)} |E_0|^2 + \epsilon_0 \chi_{2\omega}^{(2)} e^{2i\omega t} \\ + \epsilon_0 \chi_{\omega}^{(3)} E^3 e^{i\omega t} + \epsilon_0 \chi_{3\omega}^{(3)} E^3(t) e^{3i\omega t} + c.c \end{aligned} \tag{30}$$

$\chi_0^{(2)}$ ,  $\chi_{2\omega}^{(2)}$ ,  $\chi_{\omega}^{(3)}$  and  $\chi_{3\omega}^{(3)}$  are the optical rectification, the second harmonic generation (SHG), third order optical susceptibility and the third order harmonic generation (THG), respectively. The mathematical formulation of different contributions in the polarization can be derived by using the compact density matrix method. In this study, we have ignored the non-resonant terms as they have trivial contributions. We have focused on the three following effects [53, 54]:

$$\chi_{\omega}^{(1)} = \frac{\hbar\sigma}{\epsilon_0} \frac{|M_{21}|^2}{\hbar\omega - E_{21} - j\hbar\Gamma_{21}} \tag{31}$$



$$\chi_{2\omega}^{(2)} = \frac{\sigma}{\epsilon_0} \frac{M_{12}M_{23}M_{31}}{(\hbar\omega - E_{21} - j\hbar\Gamma_{21})(2\hbar\omega - E_{31} - j\hbar\Gamma_{31})} \quad (32)$$

and

$$\chi_{3\omega}^{(3)} = \frac{\sigma}{\epsilon_0} \frac{M_{12}M_{23}M_{34}M_{41}}{(\hbar\omega - E_{21} - j\hbar\Gamma_{21})(2\hbar\omega - E_{31} - j\hbar\Gamma_{31})(3\hbar\omega - E_{41} - j\hbar\Gamma_{41})} \quad (33)$$

where interstate damping terms are as follow— $\Gamma_{21} = \Gamma_f$ ,  $\Gamma_{31} = \Gamma_f/2$ , and  $\Gamma_{41} = \Gamma_f/3$ . We note that the different dipolar matrix elements  $M_{xy}$  is also called oscillator strengths between two allowed transitions  $i$  and  $f$ .

### 3 Results and discussion

The parameters used in the numerical calculations for GaN core/shell QD are as follows:  $m_c^* = 0.19m_0$ ,  $g^* = 2.06$ ,  $\epsilon = 8.9$ ,  $a^* = 2.48 \text{ nm}$ ,  $R^* = 32.62 \text{ meV}$ ,  $\Gamma_f = 0.2 \text{ ps}^{-1}$ ,  $n_r = 3.08$ ,  $I = 2 \times 10^5 \text{ W/m}^2$  and  $\sigma = 4.6 \times 10^{22} \text{ m}^{-3}$  [46, 55]. We have calculated the spectrum of CCSQD using the method described in the previous section. The energy levels and the transition matrix elements, and found that the energy levels as well as the transition matrix elements stongly depend on the material parameters and on the  $\alpha_R$  and also on the applied magnetic field  $B$ . Figure 1 shows a schematic representation of the system’s setup.

The problem of threshold magnetic field strength in semiconductor materials is related to the dimensionless parameter  $\gamma$ , ( $0 < \gamma < 1$ ). Generally speaking  $\gamma$  define the strength of the applied magnetic field: ( $\gamma \ll 1$  corresponds to

low magnetic fields) and ( $\gamma$  tend to 1 corresponds to high magnetic fields). We have already discussed this important point in our previous papers see for example [47]. The relation between  $B$ (Tesla) and  $\gamma$  writes as:  $B(T) = [(\frac{m_c^*}{m_e})\mu_B^{-1}R^*]\gamma$ , ( $\mu_B = \frac{e\hbar}{2m_e c} = 5.796 \times 10^{-2} \text{ meVT}^{-1}$  is the Bohr magneton). By using the physical parameters of GaN,  $B(T) = 106.93\gamma$ . In our case, we have choose three low values of ( $\gamma = 0.09, 0.18$  and  $0.28$ ) Which correspond to  $B = 10, 20$  and  $30 \text{ T}$ , respectively.

Figure 2 shows the variation in transition energies as a function of Rashba parameter ( $\alpha_R$ ) for  $R_c = 1a^*$  and  $R_s = 2a^*$  and height  $H = 10^*$ . Different colors represent different strength of magnetic field, i.e., black, red and blue for fields of 10T, 20T and 30T, respectively. It was observed that on increasing Rashba parameter, there is shift towards higher energy irrespective of the value of the applied magnetic field. This shifting towards higher energies is further enhanced by increasing the magnetic field, as clearly seen in the graphs.

Figure 3 represents the effect of  $\alpha_R$  on transition matrix elements of few transitions from initial ( $i$ ) to final state ( $f$ ) which are denoted by  $M_{fi}$ . The variations of matrix elements  $M_{21}$ ,  $M_{23}$ ,  $M_{34}$ ,  $M_{31}$  and  $M_{41}$  with  $\alpha_R$  for different magnetic fields are shown in Figures 3A–E, respectively. It is seen that when  $\delta_{if} = \pm 1, \pm 2$ , there is smooth variation in electric dipole moment with  $\alpha_R$ . These changes in  $M_{fi}$  can be either increasing (Figure 3A) or decreasing (Figures 3B–D). The change in  $\alpha_R$  produces a change in energy levels and wavefunctions. These changes are expected

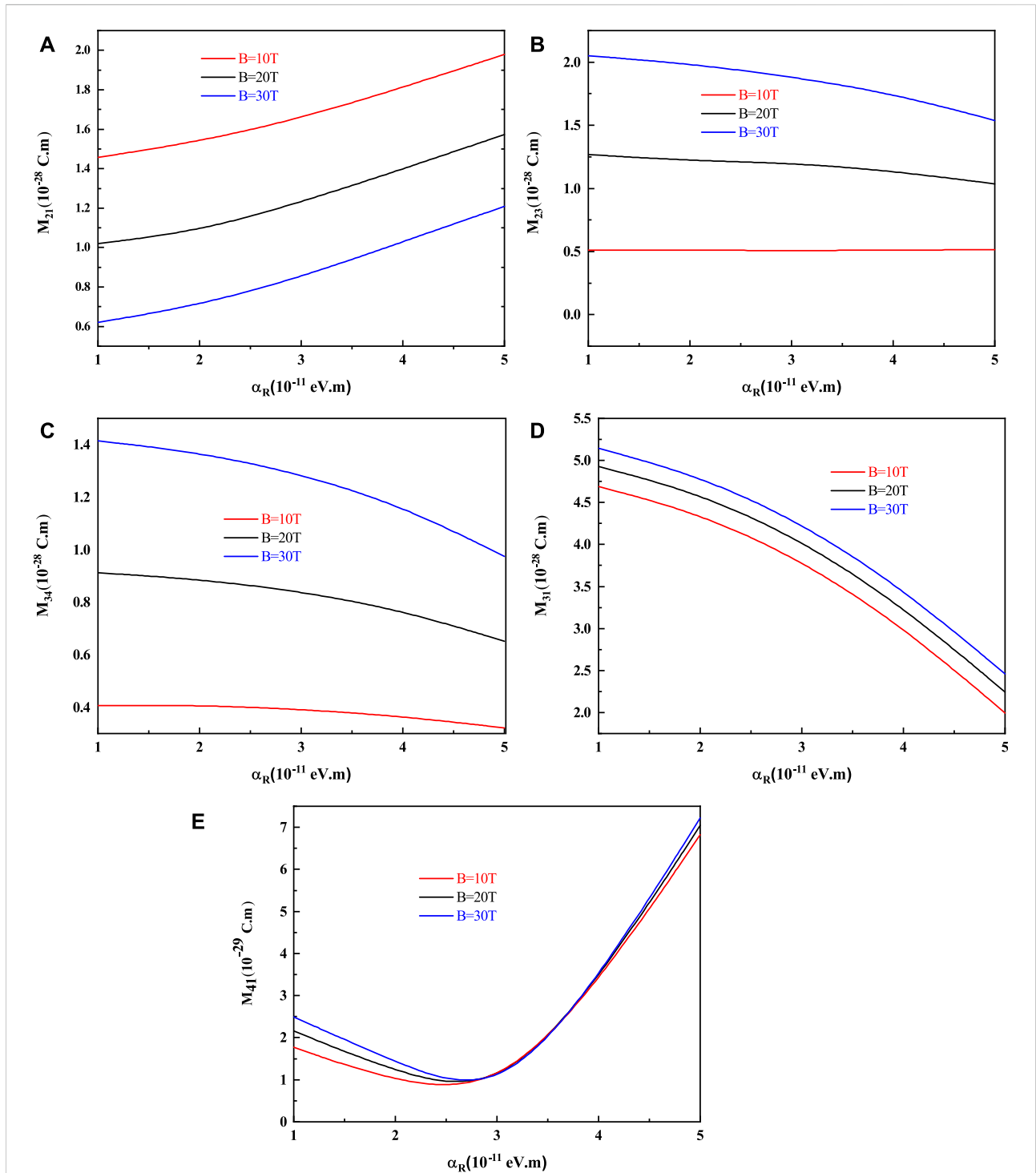
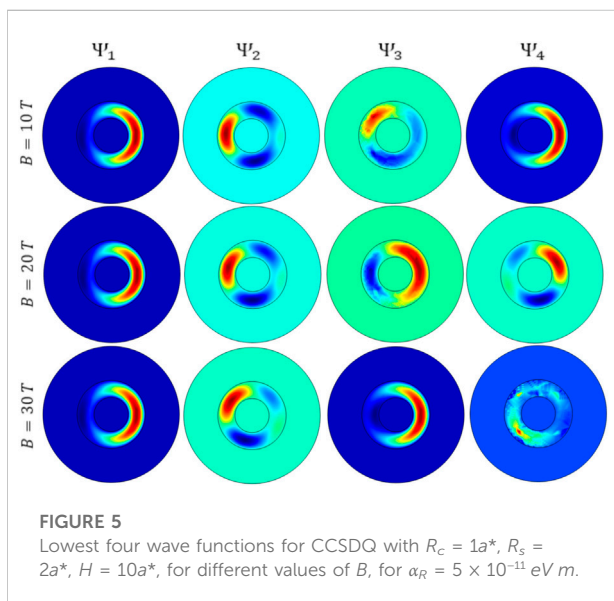
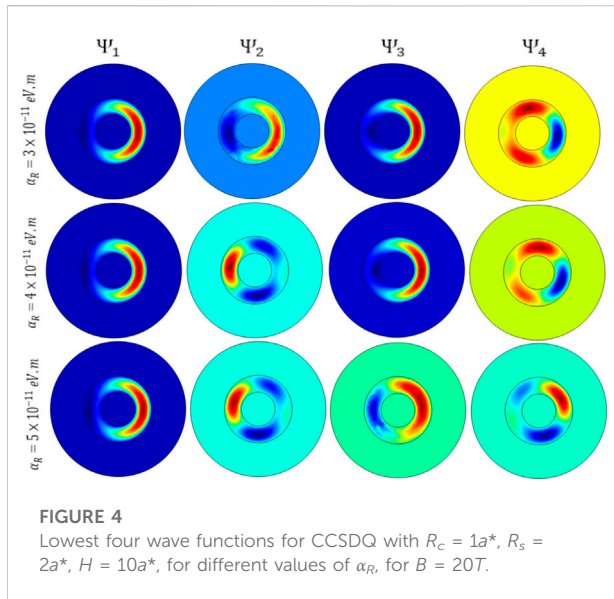


**FIGURE 3** Different matrix elements (A)  $M_{21}$ , (B)  $M_{23}$ , (C)  $M_{34}$ , (D)  $M_{31}$ , and (E)  $M_{41}$  for CCSQD with  $\alpha_R$  for different magnetic fields and  $R_c = 1a^*$ ,  $R_s = 2a^*$ , and  $H = 10a^*$ .

to be smooth in the aforementioned cases as SOI coupling remains quite small compared to other interactions. However, for  $M_{41}$ , first we see a dip with increasing  $\alpha_R$  for all magnetic fields, and then the value of the transition matrix

element increases with  $\alpha_R$  for all magnetic fields. This increase is almost the same for all strengths of magnetic field. In Figure 4, first four low-lying states of the CCSQD in the presence of different SOI strengths are shown. As shown in figure, first row



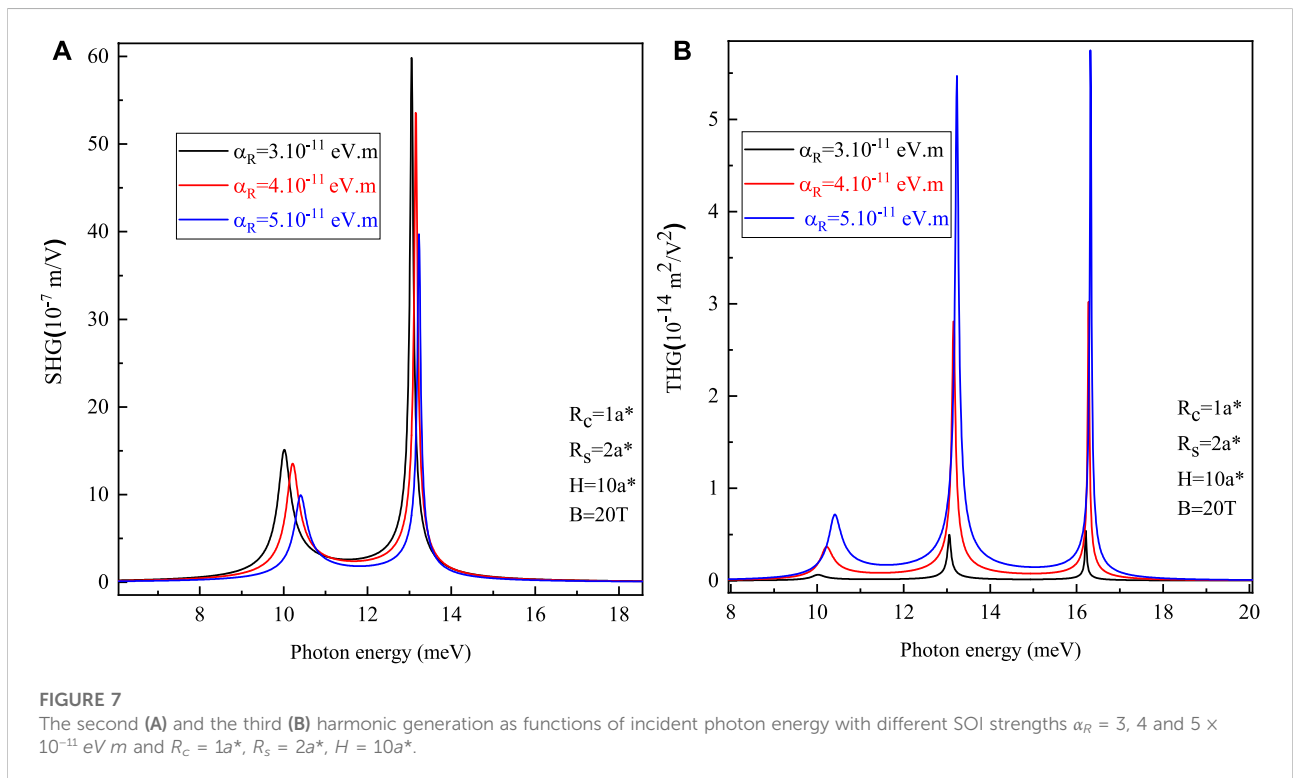
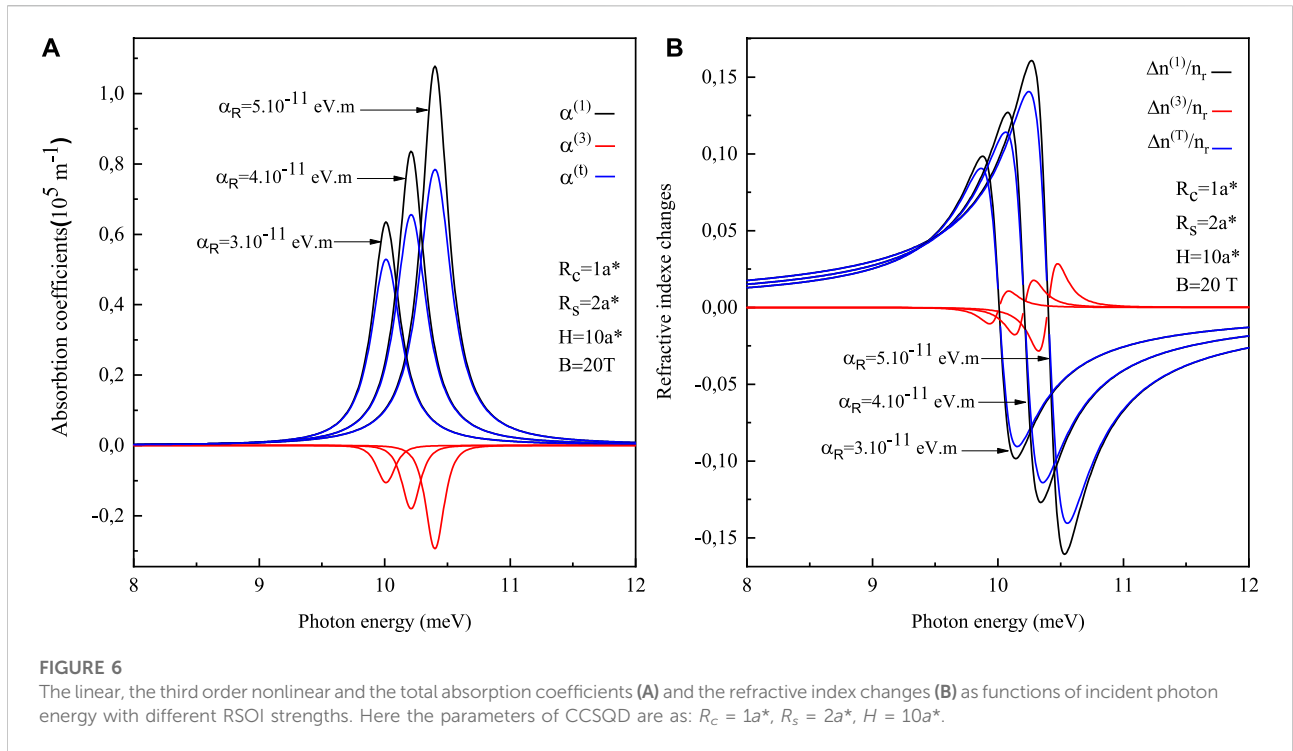
corresponds to  $\alpha_R = 3 \times 10^{-11} eV m$  and the next two rows correspond to  $\alpha_R = 4 \times 10^{-11} eV m$  and  $\alpha_R = 5 \times 10^{-11} eV m$ , respectively. We have kept the magnetic field fixed at 20T for these results. It can be seen from the figure that the wavefunctions  $\Psi_2$  and  $\Psi_4$  show more splitting compared to  $\Psi_1$  and  $\Psi_3$ . This splitting may be attributed to increased SOI effect as we increase the Rashba parameter. Figure 5 shows similar results but for different values of magnetic fields, i.e.,  $B = 10T$ ,  $B = 20T$  and  $B = 30T$ , respectively. Here, we have kept  $\alpha_R = 5 \times 10^{-11} eV m$ . Here, again, we can see that more splitting is observed in wave functions  $\Psi_2$  and  $\Psi_4$  as compared

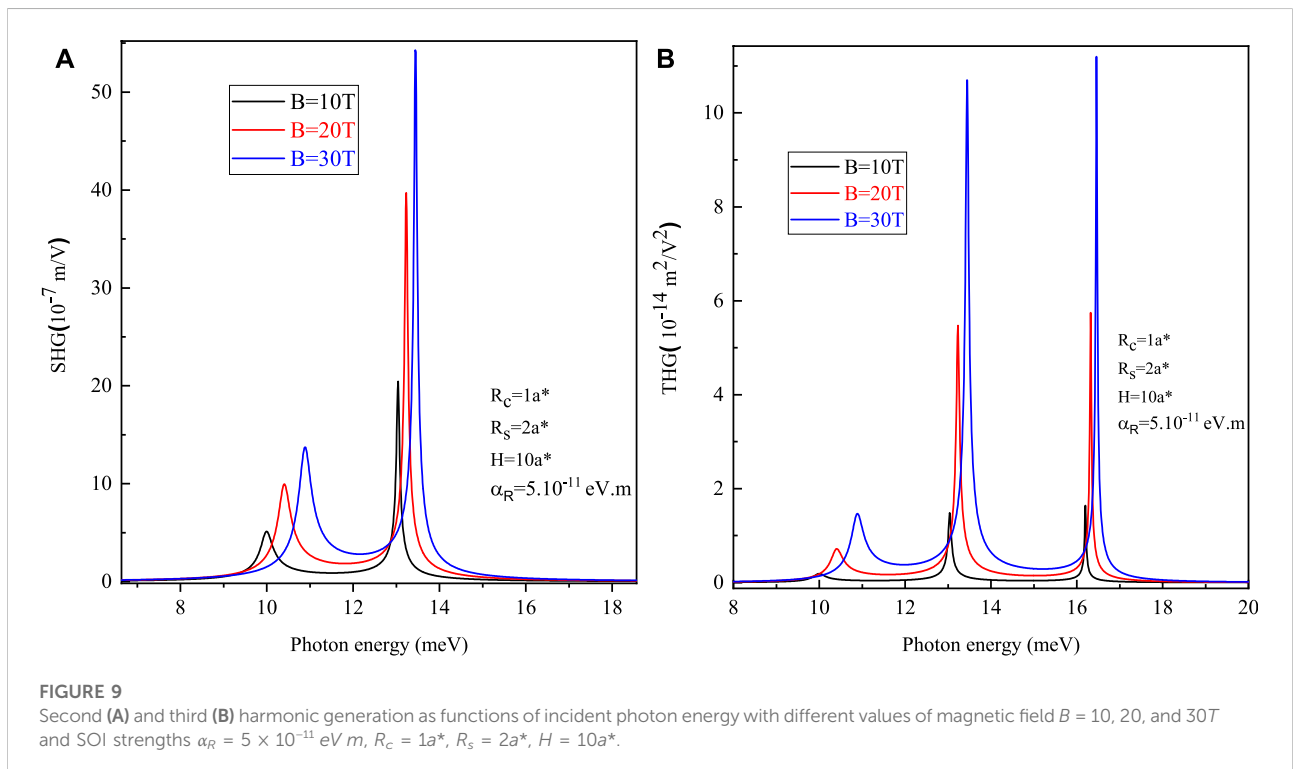
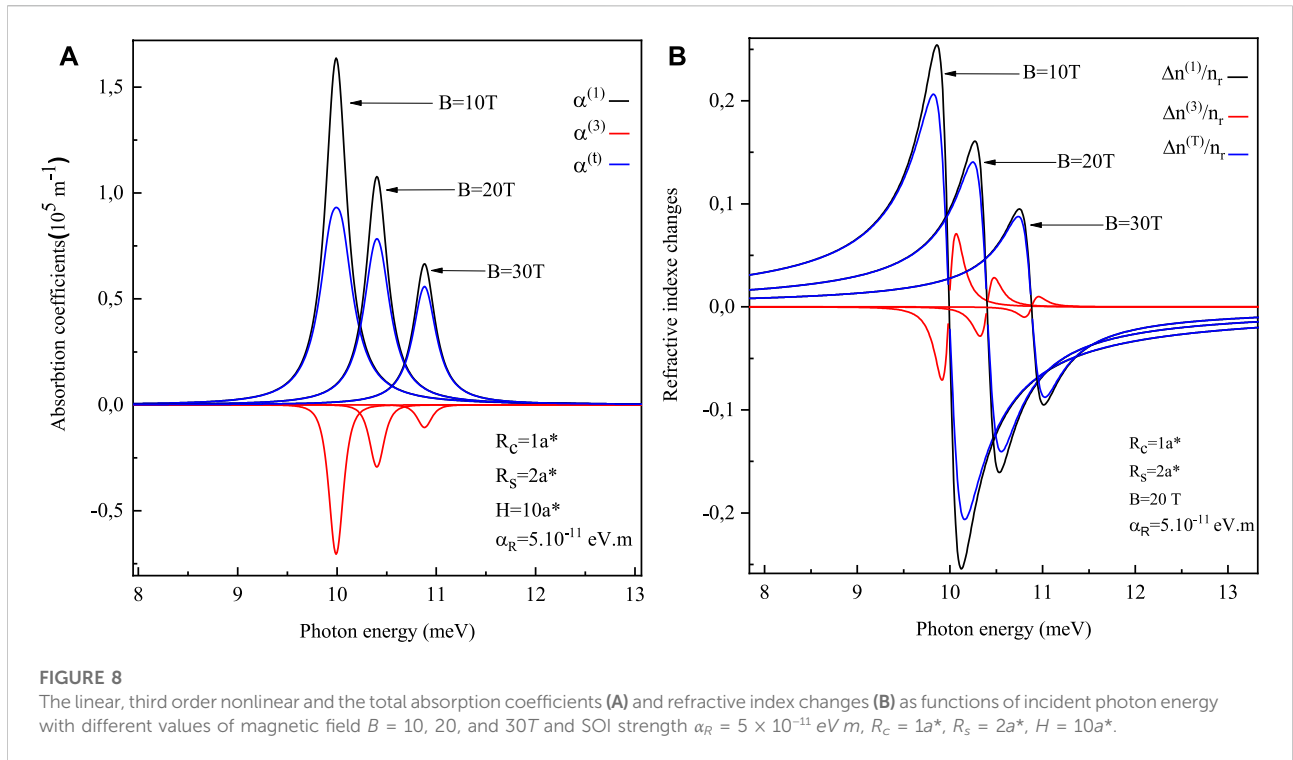
to  $\Psi_1$  and  $\Psi_3$ . This may be due to increased SOI effects due to the magnetic field.

The calculated transition energies and off-diagonal electric dipole matrix elements constitute the source of understanding the properties of the interstate optical coefficients investigated in this work. In the subsequent plots, we have investigated the behaviour of the ACs, RI changes, SHG and THG when the Rashba parameter is varied for a constant magnetic field ( $B = 20T$ ). The role of the effect of  $\alpha_R$  in the changes of AC and RI shown in Figures 6A,B. We see that the increase in  $\alpha_R$  leads to a shift towards higher energies. The reason is that the transition energy increases with the spin orbit coupling. This phenomenon is explained previously in the figure of  $E_{fi}$ , concerning the variation of the amplitude increase, due to the variation in the matrix element  $M_{21}$ . In Figure 7 we have shown the changes in SHG and THG coefficients with photon energy, again keeping the magnetic field constant at 20T for  $\alpha_R = 3, 4$  and  $5 \times 10^{-11} eV m$ . A blue shift is visible in peaks for the SHG and the THG coefficients on increasing the Rashba parameter.

In Figure 8, the variation of AC and RIC with photon energy are presented. Figures 8A,B shows the variation of AC and RIC of a CCSQD as a function of photon energy for three values of height when  $\alpha_R = 5 \times 10^{-11} eV m$ ,  $B = 20 T$ ,  $R_c = 1a^*$ ,  $R_s = 2a^*$ . It is well observed that a shift towards high energies when the height  $H$  decreases, this displacement is caused by the increase in transition energies. Moreover, it can be observed that the amplitude increases as the height increases. It is observed due to the variation of the dipole matrix element with the height. It is noticed that the magnetic field has a significant effect on AC and RIC. In Figures 6A,B, we can see that the curves show resonances when  $E_{fi}$  becomes comparable with  $\hbar\omega$ . At such energies, an increase in the magnetic field leads to a displacement of the resonances towards higher energies. This shift is due to the increased transition energy. Because as  $B$  increases, sub level energies also increase and consequently, their transition energy  $E_{21}$  also increases. By increasing energy sub-level and reducing overlap between the wave functions,  $M_{21}$  decreases and the peaks are reduced by increasing  $B$ .

In Figure 9, the variation of SHG and THG coefficients for different values of magnetic field, i.e.,  $B = 10T, 20T$  and  $30T$  for fixed value of  $\alpha_R = 5 \times 10^{-11} eV m$  with the photon energy is shown. Again, as expected, a shift towards higher energies is observed in the peaks. This is due to increase in SOI on increasing the magnetic field. In Figure 10, we studied the linear, the third order nonlinear and the total ACs and RICs as a function of photon energy for different heights ( $H$ ). Here we keep the magnetic field and Rashba parameter fixed. It is well observed that there is a shift towards higher energies when the height  $H$  decreases, This change is caused by the increase in transition energies. Moreover, it can be observed that the amplitude decreases as the height increases. This can be explained to be happening due to the variation of the dipole matrix element with the height.





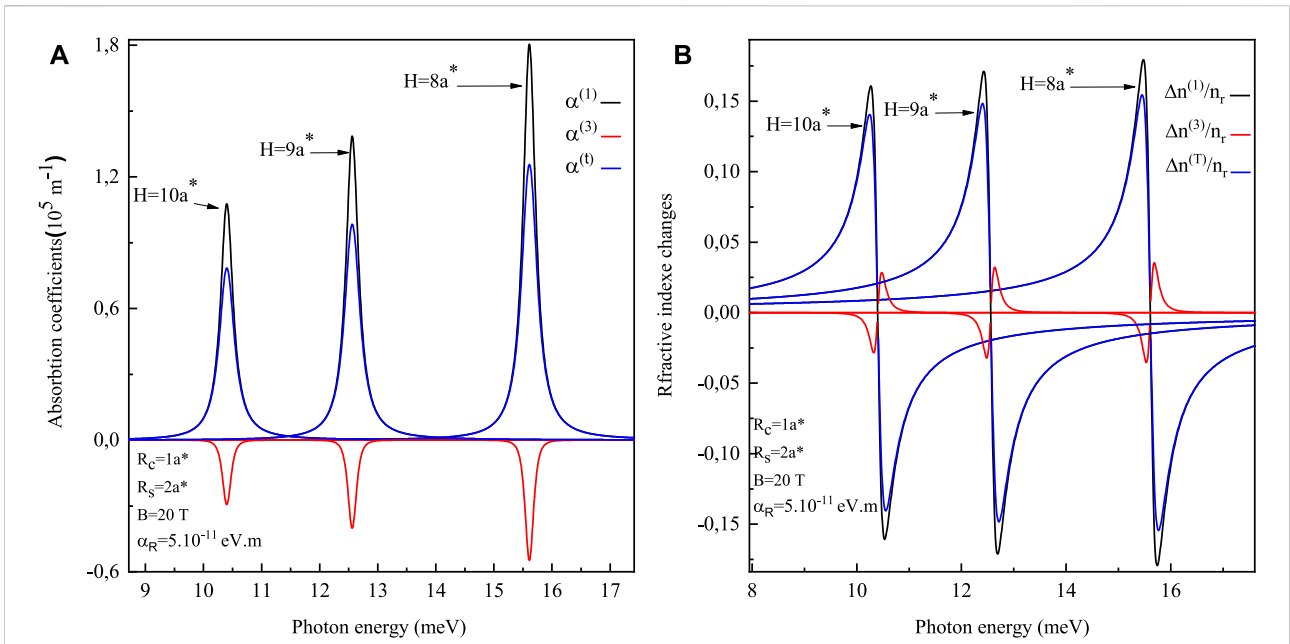


**FIGURE 10**  
The linear, the third order nonlinear and the total absorption coefficients (A) and refractive index changes (B) as functions of incident photon energy for different heights  $H = 8, 9$  and  $10a^*$  of the CCSQD with  $R_c = 1a^*$ ,  $R_s = 2a^*$ . The SOI strength is  $\alpha_R = 5 \times 10^{-11} \text{ eV.m}$ , and  $B = 20 \text{ T}$

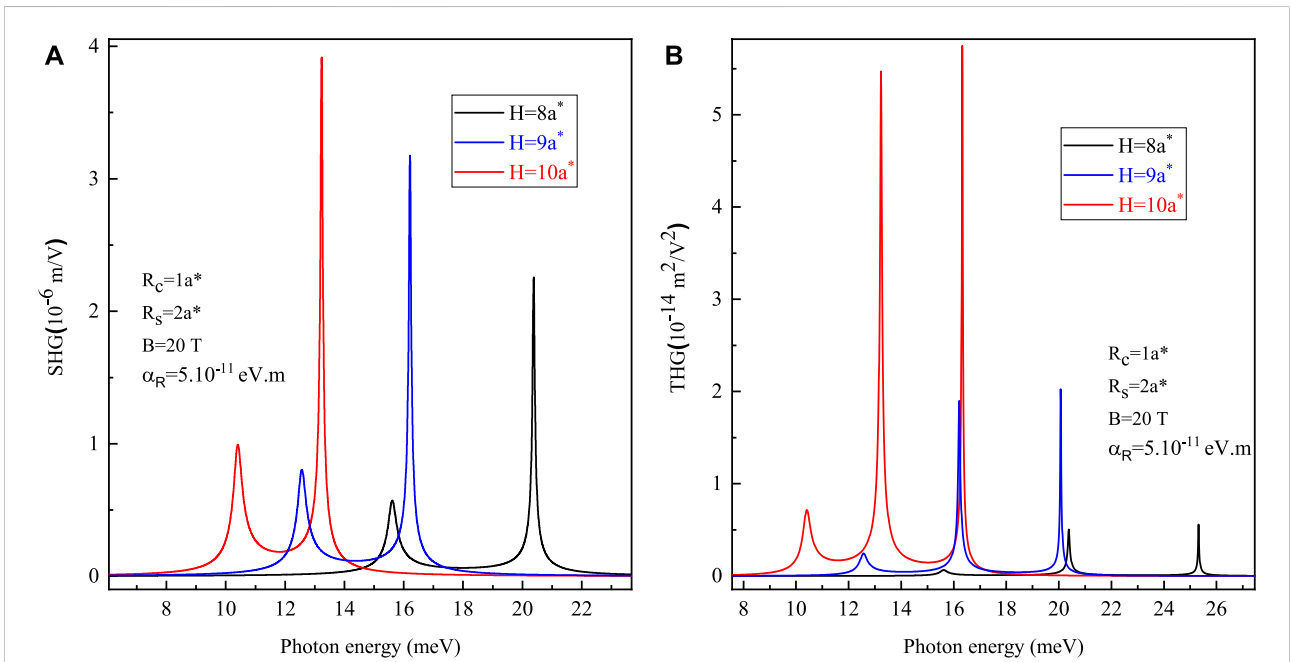


**FIGURE 11**  
The Second ahrmonic generation (A) and third harmonic generation (B) as function of incident photon energy with different heights  $H = 8, 9$  and  $10a^*$  of the CCSQD for  $\alpha_R = 5 \times 10^{-11} \text{ eV.m}$ ,  $R_c = 1a^*$ ,  $R_s = 2a^*$ ,  $B = 20 \text{ T}$ .

In Figure 11, we studied the variation of SHG and THG for different values of H, again keeping magnetic field and Rashba parameter fixed at constant values. Here, we observed variations similar to Figure 10. It is noticed again that there is a shift towards higher energies when the height H decreases. But here, unlike ACs and RICs, amplitude is found to increase with the increase in height H.

## 4 Conclusion

In this study, we have investigated the influence of Rashba spin orbit interaction on an electron in cylindrical core/shell quantum dot. The transition energy changes significantly when we vary the Rashba parameter and magnetic field. When we increase the magnetic field or Rashba parameter, a shift towards higher energies is observed in transition energies. Variations in the Rashba coupling parameter, magnetic field, and effective Rydberg energy also cause measurable changes in the systems linear and nonlinear optical properties. As we increase the magnetic field, peaks of the absorption coefficients and refractive index changes show a blue shift. Second and third harmonic generation peaks also show shifts towards higher values of energy on increasing the magnetic field and Rashba parameter. Through our results, we have shown that it is possible to manipulate the above-mentioned properties of cylindrical core/shell quantum dots by utilizing the Rashba spin orbit coupling effects that become dominant as we increase the magnetic field. For requirements for a specific article type please refer to the Article Types on any Frontiers journal page. Please also refer to Author Guidelines for further information on how to organize your manuscript in the required sections or their equivalents for your field.

## Data availability statement

The data presented in this study are available on reasonable request to the corresponding author.

## References

- Chang LL, Leo E. Semiconductor quantum heterostructures. *Phys Today* (1992) 45:10:36–43. doi:10.1063/1.881342
- Ohya S, Nam Hai P, Mizuno Y, Phys MT. Quantum size effect and tunneling magnetoresistance in ferromagnetic-semiconductor quantum heterostructures. *Phys Rev B* (2007) 75:155328. doi:10.1103/physrevb.75.155328
- Alferov ZHL. The history and future of semiconductor heterostructures. *Semiconductors* (1998) 32:1–14. doi:10.1134/1.1187350
- Nolte DD. Semi-insulating semiconductor heterostructures: optoelectronic properties and applications. *J Appl Phys* (1999) 85:6259–89. doi:10.1063/1.370284
- Li X, Chen W, Zhang S, Wu Z, Wang P, Xu Z, et al. 18.5% efficient graphene/GaAs van der waals heterostructure solar cell. *Nano Energy* (2015) 16:310–9. doi:10.1016/j.nanoen.2015.07.003
- Hsu KC, Fang TH, Hsiao YJ, Wu PC. Response and characteristics of TiO<sub>2</sub>/perovskite heterojunctions for CO gas sensors. *J Alloys Compd* (2019) 794:576–84. doi:10.1016/j.jallcom.2019.04.238
- Feng M, Holonyak N, Jr, Chan R. Quantum-well-base heterojunction bipolar light-emitting transistor. *Appl Phys Lett* (2004) 84:1952–4. doi:10.1063/1.1669071
- Pierre A, Gaikwad A, Arias AC. Charge-integrating organic heterojunction phototransistors for wide-dynamic-range image sensors. *Nat Photon* (2017) 11:193–9. doi:10.1038/nphoton.2017.15
- Low J, Yu J, Jaroniec M, Wageh S, Al-Ghamdi AA. Heterojunction photocatalysts. *Adv Mater* (2017) 29:1601694. doi:10.1002/adma.201601694
- Edvinsson T. Optical quantum confinement and photocatalytic properties in two-one- and zero-dimensional nanostructures. *R Soc open Sci* (2018) 5:180387. doi:10.1098/rsos.180387
- Sangwan VK, Hersam MC. Neuromorphic nanoelectronic materials. *Nat Nanotechnol* (2020) 15:517528–8. doi:10.1038/s41565-020-0647-z
- Rossi F. Coherent phenomena in semiconductors. *Semicond Sci Technol* (1998) 13:147–68. doi:10.1088/0268-1242/13/2/001

## Author contributions

Conceptualization, LMP, VP, and EF; data curation, MK; formal analysis, VN and MK; methodology, KL, V, and JE; project administration, EF, VP, and DL; resources, DL; software, MK, VN, and JE; supervision, EF, VP, and DL; validation, LMP, VP, DL, and EF; visualization, LMP, KL, DL, and EF; writing—original draft, MK, GL, and VN; writing—review and editing, VN, VP, DL, and EF. All authors have read and agreed to the published version of the manuscript.

## Funding

LMP acknowledges financial support from ANID through Convocatoria Nacional Subvención a Instalación en la Academia Convocatoria Año 2021, Grant SA77210040. DL acknowledges partial financial support from Centers of Excellence with BASAL/ANID financing Grant AFB180001, CEDENNA.

## Conflict of interest

The authors declare that the research was conducted in the absence of any commercial or financial relationships that could be construed as a potential conflict of interest.

## Publisher's note

All claims expressed in this article are solely those of the authors and do not necessarily represent those of their affiliated organizations, or those of the publisher, the editors, and the reviewers. Any product that may be evaluated in this article, or claim that may be made by its manufacturer, is not guaranteed or endorsed by the publisher.

13. De Rinaldis S, D Amico I, Biolatti E, Rinaldi R, Cingolani R, Rossi F, et al. Intrinsic exciton-exciton coupling in GaN-based quantum dots: application to solid-state quantum computing. *Phys Rev B* (2002) 65:081309. doi:10.1103/physrevb.65.081309
14. Biolatti E, D Amico I, Zanardi P, Rossi F. Electro-optical properties of semiconductor quantum dots: application to quantum information processing. *Phys Rev B* (2002) 65:075306. doi:10.1103/physrevb.65.075306
15. Nautiyal V, Munjal D, Sotia P. *J Magn Magn Mater* (2021) 528:167688.
16. Kria M, Farkous M, Prasad V, Dujardin F, Pérez ML, Laroze D, et al. *Curr Appl Phys* (2021) 25:1
17. Loss D, DiVincenzo DP. Quantum computation with quantum dots. *Phys Rev A (Coll Park)* (1998) 57:120–6. doi:10.1103/physreva.57.120
18. Gao X, Cui Y, Levenson R, Chung LE, Nie S. *In vivo* cancer targeting and imaging with semiconductor quantum dots. *Nat Biotechnol* (2004) 22:969–76. doi:10.1038/nbt994
19. Hu YZ, Koch SW, Lindberg M, Peyghambarian N, Pollock EL, Abraham FF, et al. Biexcitons in semiconductor quantum dots. *Phys Rev Lett* (1990) 64:1805–7. doi:10.1103/physrevlett.64.1805
20. Yamijala SS, Mukhophadey SM, Pati SK. Linear and nonlinear optical properties of graphene quantum dots: a computational study. *J Phys Chem C* (2015) 119:12079–87. doi:10.1021/acs.jpcc.5b03531
21. Schmitt-Rink S, Miller DAB, Chemla DS. *Phys Rev B* (1987) 35:8113.
22. Kondratenko TS, Zvyagin AI, Smirnov MS, Grevtseva G, P erelitsa AS, Ovchinnikov OV, et al. Luminescence and nonlinear optical properties of colloidal Ag<sub>2</sub>S quantum dots. *J Lumin* (2019) 208:193–200. doi:10.1016/j.jlumin.2018.12.042
23. Niculescu EC, Bejan D. Off-centre impurity-related nonlinear optical absorption, second and third harmonic generation in a two-dimensional quantum ring under magnetic field. *Philos Mag* (2017) 97:2089–107. doi:10.1080/14786435.2017.1323130
24. Zeng Z, Garoufalos CS, Terzis AF, Baskoutas S. Linear and nonlinear optical properties of ZnO/ZnS and ZnS/ZnO core shell quantum dots: effects of shell thickness, impurity, and dielectric environment. *J Appl Phys* (2013) 114:023510. doi:10.1063/1.4813094
25. Zhu H, Song N, Lian T. Controlling charge separation and recombination rates in CdSe/ZnS type I core-shell quantum dots by shell thicknesses. *J Am Chem Soc* (2010) 132:15038–45. doi:10.1021/ja106710m
26. Vasudevan D, Gaddam RR, Trinchi A, Cole I. Core-shell quantum dots: properties and applications. *J Alloys Compd* (2015) 636:395–404. doi:10.1016/j.jallcom.2015.02.102
27. Aghoutane N, El Yadri M, El Aouami A, Feddi E, Long G, Sadoqi M, et al. Excitonic nonlinear optical properties in AlN/GaN spherical core/shell quantum dots under pressure. *MRS Commun* (2019) 9:663. doi:10.1557/mrc.2019.43
28. Han W, Kawakami KR, Gmitra M, Fabian J. *Nat Techn* (2014) 9:794–807. doi:10.1038/nnano.2014.214
29. Premasiri K, Gao XPA. Tuning spin-orbit coupling in 2D materials for spintronics: a topical review. *J Phys : Condens Matter* (2019) 31:193001. doi:10.1088/1361-648x/ab04c7
30. Ceferino A, Magorrian SJ, Zolyomi V, Bandurin DA, Geim AK, Patane A, et al. Tunable spin-orbit coupling in two-dimensional InSe. *Phys Rev B* (2021) 104:125432. doi:10.1103/physrevb.104.125432
31. Winkler R. *Spin-orbit coupling effects in two-dimensional electron and hole systems*, 191. New York, NY: Springer (2003).
32. Pourmand SE, Rezaei G, Vaseghi B. Impacts of external fields and Rashba and Dresselhaus spin-orbit interactions on the optical rectification, second and third harmonic generations of a quantum ring. *Eur Phys J B* (2019) 92:96. doi:10.1140/epjb/e2019-90717-6
33. Lakaal K, Kria M, El Hamdaoui J, VarshaPrasad V, Nautiyal VV, et al. Polaronic corrections on magnetization and thermodynamic properties of electron-electron in 2D systems with Rashba spin-orbit coupling. *J Magn Magn Mater* (2022) 551:169042. doi:10.1016/j.jmmm.2022.169042
34. Gharati A. *Solid State Commun* (2017) 38:30122–9.
35. Vaseghi B, Rezaei G, Malian M. Energy levels and electron g-factor of spherical quantum dots with Rashba spin-orbit interaction. *Phys Lett A* (2011) 375:2747–53. doi:10.1016/j.physleta.2011.06.011
36. Vaseghi n B, Rezaei G, Malian M. Spin-orbit interaction effects on the optical properties of spherical quantum dot. *Opt Commun* (2013) 287:241–4. doi:10.1016/j.optcom.2012.09.039
37. Sun P, Li Y, Meng X, Yu S, Liu Y, Liu F, et al. The magnetic field effect on optical properties of Sm-doped GaN thin films. *J Mater Sci Mater Electron* (2014) 25:2974–8. doi:10.1007/s10854-014-1969-0
38. Mkrtchyan MA, Hayrapetyan DB, Kazaryan EM, Sarkisyan HA, Vinnichenko MY, Shalygin VA, et al. Effects of an external magnetic field on the interband and intraband optical properties of an asymmetric biconvex lens-shaped quantum dot. *Nanomaterials* (2021) 12:60. doi:10.3390/nano12010060
39. Dong Y, Sun W, Huang C, Huang S, Yan C, Wen J, et al. Influence of particle size on the magneto-refractive effect in PbS quantum dots-doped liquid core fiber. *Opt Mater Express* (2022) 12:1838. doi:10.1364/ome.456622
40. Mommadi O, El Moussaouy A, Chnafi M, El Hadi M, Nougaoui A, Magrez H, et al. Exciton-phonon properties in cylindrical quantum dot with parabolic confinement potential under electric field. *Physica E: Low-dimensional Syst Nanostructures* (2020) 118:113903. doi:10.1016/j.physe.2019.113903
41. Deimert C, Wasilewski ZR. MBE growth of continuously-graded parabolic quantum well arrays in AlGaAs. *J Cryst Growth* (2019) 514:103–8. doi:10.1016/j.jcrysgro.2019.02.045
42. Kappell M, Turck V, Grundmann M, Cerva H, Bimberg D. Low pressure metal-organic chemical vapor deposition of InP/InAlAs/InGaAs quantum wires. *J Cryst Growth* (1997) 170:590–4. doi:10.1016/s0022-0248(96)00612-4
43. Iorio A, Rocci M, Bours L, Carrega M, Zannier V, Sorba L, et al. Vectorial control of the spin-orbit interaction in suspended InAs nanowires. *Nano Lett* (2018) 19:652–7. doi:10.1021/acs.nanolett.8b02828
44. Voon LY, Lok C. Physical properties of silicene. In: *Silicene*. Cham: Springer (2016). p. 3–33.
45. Van Weperen I, Tarasinski B, Eeltink D, Pribragi V, Plissard SR, Bakkers EPAM, et al. Spin-orbit interaction in InSb nanowires. *Phys Rev B* (2015) 91:201413. doi:10.1103/physrevb.91.201413
46. Oshima Y, Yoshida T, Watanabe K, Mishima T. Properties of Ge-doped, high-quality bulk GaN crystals fabricated by hydride vapor phase epitaxy. *J Cryst Growth* (2010) 312:3569–73. doi:10.1016/j.jcrysgro.2010.09.036
47. El Khamkhami J, Feddi E, Assaid E, Dujardin F, Stébe B, El Haouari M, et al. Magneto-bound polaron in CdSe spherical quantum dots: strong coupling approach. *Physica E: Low-dimensional Syst Nanostructures* (2005) 25:366–73. doi:10.1016/j.physe.2004.06.059
48. Kria M, El-Yadri M, Aghoutane N, Pérez LM, Laroze D, Feddi E. *Chin J Phys* (2020) 66:444.
49. Yu YB, Wang HJ. Third-harmonic generation in two-dimensional pseudo-dot system with an applied magnetic field. *Superlattices Microstruct* (2011) 50:252–60. doi:10.1016/j.spmi.2011.07.001
50. Boyd RW. *Nonlinear Optics*. 2nd ed. Academic Press (2003).
51. Vahdani MRK, Rezaei G. Linear and nonlinear optical properties of a hydrogenic donor in lens-shaped quantum dots. *Phys Lett A* (2009) 373:3079–84. doi:10.1016/j.physleta.2009.06.042
52. Vahdani MRK, Rezaei G. Intersubband optical absorption coefficients and refractive index changes in a parabolic cylinder quantum dot. *Phys Lett A* (2010) 374:637–43. doi:10.1016/j.physleta.2009.11.038
53. Shahzadeh M, Sabaeian M. A comparison between semi-spheroid- and dome-shaped quantum dots coupled to wetting layer. *AIP Adv* (2014) 4:067134. doi:10.1063/1.4885135
54. Sabaeian M, Shahzadeh M, Farbod M. Electric field-induced nonlinearity enhancement in strained semi-spheroid-shaped quantum dots coupled to wetting layer. *AIP Adv* (2014) 4:127105. doi:10.1063/1.4903368
55. Levinshtein ME, Rumyantsev SL, Shur MS. *Properties of advanced semiconductor materials: GaN, AlN, InN, BN, SiC, SiGe*. John Wiley & Sons (2001).